

# Stacking-dependent magnetic ordering in bilayer $\text{ScI}_2$

Soumyajit Sarkar\* and Soham Chandra

*Department of Physics, Brainware University, Barasat, Kolkata-700125, India*

(Dated: February 13, 2026)

Stacking-dependent magnetism in two-dimensional van der Waals materials offers an effective route for controlling magnetic order without chemical modification. Here, we present a combined first-principles and finite-temperature study of magnetic ordering in bilayer  $\text{ScI}_2$  with different stacking configurations. Using density functional theory with Hubbard- $U$  corrections, we investigate the structural, electronic, and magnetic properties of monolayer and bilayer  $\text{ScI}_2$  in AA, AB, and BA stackings. The electronic structure exhibits a spin-polarized ground state dominated by  $\text{Sc-}d$  states near the Fermi level. Mapping total energies onto an effective Heisenberg spin Hamiltonian reveals strong intralayer ferromagnetic exchange that is largely insensitive to stacking, while the interlayer exchange depends strongly on stacking geometry, favoring ferromagnetic coupling for AA and BA stackings and antiferromagnetic coupling for the AB stacking. Spin-orbit coupling calculations show that both monolayer and bilayer  $\text{ScI}_2$  possess a robust out-of-plane magnetic easy axis. Finite-temperature Monte Carlo simulations indicate that all bilayer configurations sustain magnetic ordering at and above room temperature, with ordering temperatures in the range 360–375 K, as confirmed by Binder cumulant analysis and finite-size scaling. These results demonstrate that stacking geometry enables control of the magnetic ground state in bilayer  $\text{ScI}_2$  without significantly affecting its thermal stability.

**Keywords:** Two-dimensional magnetism, van der Waals bilayers, Density functional theory, First-principles calculations, Monte Carlo simulations,  $\text{ScI}_2$

## I. INTRODUCTION

The discovery of intrinsic magnetism in two-dimensional (2D) van der Waals (vdW) materials has revolutionized the field of condensed matter physics, offering unprecedented opportunities for exploring low-dimensional quantum phenomena and developing next-generation spintronic devices [1]. These atomically thin magnets, such as  $\text{CrI}_3$  and  $\text{Fe}_3\text{GeTe}_2$ , exhibit long-range magnetic order down to the monolayer limit, challenging traditional theories like the Mermin-Wagner theorem by incorporating magnetic anisotropy to stabilize ordering against thermal fluctuations[1, 2]. Layer-dependent magnetic properties are prominent in these systems, as evidenced by the transition from intralayer ferromagnetic (FM) ordering in monolayers to interlayer antiferromagnetic (AFM) coupling in  $\text{CrI}_3$  bilayers[3, 4] and enhanced interlayer FM exchange in  $\text{Fe}_3\text{GeTe}_2$  with decreasing layer thickness[5]. In multilayer structures, the interlayer magnetic coupling—whether FM or AFM—plays a crucial role in determining the overall magnetic behavior, with applications in magnetic tunneling junctions, memory devices, and quantum computing[6].

A key challenge in 2D magnetism is the precise control of interlayer interactions without invasive methods like doping or external fields. Recent studies have demonstrated that stacking configurations, including sliding and rotation, can profoundly influence interlayer exchange coupling in vdW bilayers[7]. For instance, in  $\text{CrBr}_3$  bilayers, direct observations via scanning tunneling microscopy revealed stacking-dependent transitions

between FM and AFM states, attributed to variations in superexchange pathways mediated by halide anions[8, 9]. Similarly, in  $\text{CrI}_2$  systems, theoretical investigations have shown that reversed stacking can induce altermagnetism or ferroelectric properties, highlighting the sensitivity of magnetic order to interlayer registry[10]. A recent theoretical study further illustrates how interlayer exchange coupling can drive magnetic phase transitions between ferromagnetism and altermagnetism in 2D lattices[11]. These findings emphasize the role of superexchange interactions, where orbital hopping between magnetic ions via non-magnetic ligands dictates the sign and strength of magnetic coupling, as described by the Goodenough-Kanamori rules[12, 13].

Despite these advances, many 2D magnetic materials remain underexplored, particularly those with unconventional stoichiometries like  $\text{AB}_2$ -type structures[14]. Scandium diiodide ( $\text{ScI}_2$ ), a predicted 2D material with intrinsic FM ordering within each layer, represents a promising candidate for tunable magnetism due to its vdW nature and potential for structural manipulation[15]. However, the interlayer magnetic behavior in bilayer  $\text{ScI}_2$ , especially under varying stacking modes, has not been systematically investigated. Understanding how sliding and rotation alter superexchange mechanisms could unlock new strategies for mechanical or electrostatic control of magnetic states.

In this work, we employ first-principles density functional theory (DFT) calculations to elucidate the stacking-dependent interlayer magnetic coupling in 2D bilayer  $\text{ScI}_2$ . We demonstrate that AA stacking favors FM coupling, while a translational shift (AB/BA) enable reversible switching between FM and AFM states, driven by orbital hopping variations. These insights reveal the

\* dss.ph@brainwareuniversity.ac.in

intricate tunability of magnetic ordering in  $\text{ScI}_2$  bilayers. The manuscript begins with a description of the computational methodology employed. This is followed by a comprehensive presentation of the results, focusing on the structural properties and magnetic couplings, along with a detailed discussion of the underlying physical mechanisms. The manuscript concludes with a summary of the key findings and an outline of their broader implications and potential directions for future research.

## II. COMPUTATIONAL DETAILS

All first-principles calculations in this study were performed using the plane-wave pseudopotential method based on density functional theory (DFT) as implemented in the Quantum ESPRESSO package [16, 17]. The exchange-correlation interaction was treated within the framework of the generalized gradient approximation (GGA) using the Perdew–Burke–Ernzerhof (PBE) functional [18].

The projector augmented-wave (PAW) method [19] was employed to describe the electron-ion interactions, with pseudopotentials taken from the standard Quantum ESPRESSO pseudopotential library. The total energies are relaxed to  $3 \times 10^{-7}$  eV/cell and crystal structures (all degrees of freedom, atomic positions, and cell) until forces on ions are below 0.005 eVÅ. Brillouin zone integration was carried out using a Monkhorst–Pack  $13 \times 13 \times 1$   $k$ -point grid [20]. A vacuum layer of at least 15Å was applied along the direction out of the plane to avoid spurious interactions between periodic images of the  $\text{ScI}_2$  monolayer or bilayers. To properly describe the localized Sc 3d electrons, we employed the DFT+ $U$  method in the Dudarev formulation[21], in which only the effective parameter  $U_{\text{eff}} = U - J$  is required. An on-site Coulomb correction of  $U_{\text{eff}} = 1.7$  eV was applied to the Sc 2d states. This choice is consistent with earlier first-principles studies on Sc-based halide monolayers and related two-dimensional transition-metal systems, where  $U_{\text{eff}}$  values in the range of 2 eV have been found to correctly capture the electronic and magnetic properties[22]. Long-range dispersion interactions were accounted for using the Grimme DFT-D3[23] van der Waals correction as implemented in QUANTUM ESPRESSO.

The thermodynamic stability of the  $\text{ScI}_2$  monolayer was assessed by computing the formation energy with respect to its constituent elements. We performed classical Monte Carlo simulations to investigate the thermomagnetic properties of bilayer  $\text{ScI}_2$  configurations. The simulations were carried out on square lattices of linear dimensions  $L = 30, 40, 50, 60, 70, 80, 100, 120, 140, 160$  and 200, with periodic boundary conditions applied along the in-plane directions. Spin configurations were updated using the local Metropolis algorithm, where trial moves are accepted with probability,  $p = \min \left\{ 1, \exp \left( -\frac{\Delta E}{k_B T} \right) \right\}$ . At each temperature, the system

was equilibrated for  $5 \times 10^4$  Monte Carlo sweeps per spin (MCSS), followed by an additional  $5 \times 10^4$  MCSS over which thermal averages were computed. To improve statistical accuracy, all reported quantities were further averaged over 10 microscopically distinct but macroscopically equivalent realizations. The sublayered magnetization i.e. magnetization per spin of the individual layers, is defined as:

$$m_{\text{top}} = \left\langle \frac{1}{N_{\text{Sc}}} \sum_{i \in \text{top}} S_i \right\rangle \quad (1)$$

$$m_{\text{bot}} = \left\langle \frac{1}{N_{\text{Sc}}} \sum_{i \in \text{bot}} S_i \right\rangle \quad (2)$$

For the ferromagnetic configurations the total magnetization,  $m_t$ , is the order parameter, and is defined as:

$$m_t = \frac{1}{2} |m_{\text{top}} + m_{\text{bot}}| \quad (3)$$

For the antiferromagnetic configuration the staggered magnetization,  $m_s$ , is the order parameter, and is defined as [24]:

$$m_s = \frac{1}{2} |m_{\text{top}} - m_{\text{bot}}| \quad (4)$$

and the magnetic susceptibility is calculated by:

$$\chi_m = \frac{1}{k_B T} (\langle m_{t,s}^2 \rangle - \langle m_{t,s} \rangle^2), \quad (5)$$

whose peak provides a preliminary estimate of the magnetic transition temperature. To obtain a size-independent and more precise determination of the critical temperature, we compute the fourth-order Binder cumulant

$$U_L = 1 - \frac{\langle m_{t,s}^4 \rangle}{3 \langle m_{t,s}^2 \rangle^2}, \quad (6)$$

for all system sizes and identify the transition temperature from the crossing points of  $U_L(T)$  curves for successive system-size pairs,  $(L, 2L)$ . The analysis is restricted to the temperature window  $355 \text{ K} \leq T \leq 385 \text{ K}$ , and only the first crossing within this range is retained to avoid spurious numerical artifacts and finite-size effects.

## III. RESULTS AND DISCUSSIONS

### A. Structural Properties of Monolayer and Bilayer $\text{ScI}_2$

#### *Monolayer Geometry*

Monolayer scandium diiodide ( $\text{ScI}_2$ ) can crystallize in two possible polymorphs distinguished by the local co-ordination environment of the Sc atoms—namely, the

*octahedral* (1T) and *trigonal prismatic* (1H) structures. Both are derived from the CdI<sub>2</sub>-type layered structure, common among transition-metal dihalides, and consist of Sc layers sandwiched between two iodine planes forming an I-Sc-I trilayer.

In the 1T phase, Sc atoms are octahedrally coordinated by six I atoms, forming edge-sharing ScI<sub>6</sub> octahedra arranged in a hexagonal lattice with space group *P-3m1*. This configuration is analogous to that found in monolayer CrI<sub>2</sub> [4]. In contrast, the 1H phase exhibits trigonal prismatic coordination of Sc by I atoms (space group *P6<sub>3</sub>/mmc*), similar to that of MoS<sub>2</sub> and other transition-metal dichalcogenides [25]. The two phases differ primarily in the stacking of I-Sc-I layers and the symmetry of the coordination environment. Our total energy calculations indicate that the 1T phase of ScI<sub>2</sub> is energetically more favorable than the 1H phase by approximately  $\Delta E \approx 0.11$  eV per formula unit. This energetic preference arises from the smaller crystal-field splitting and better overlap between Sc 3d and I 5p orbitals in the octahedral coordination, leading to a more stable electronic configuration[13]. The optimized lattice constant of the 1T monolayer is about  $a = 3.9$  Å, and the Sc-I bond length is 2.8 Å. For comparison, the 1H phase relaxes to a slightly larger lattice constant due to reduced in-plane orbital overlap.

The variety of stacking registries provides a natural platform to modulate interlayer orbital overlap and superexchange pathways between adjacent Sc layers. These geometric variations, as will be shown in the following subsections, lead to significant changes in the interlayer magnetic coupling, allowing the system to switch between ferromagnetic (FM) and antiferromagnetic (AFM) alignments through controlled stacking translations or rotations.

### Bilayer Stacking Configurations

The bilayer ScI<sub>2</sub> structures were built using the energetically favorable 1T phase as the building block. We consider three different stacking configurations based on the ground-state 1T monolayer structure: AA, AB, and BA. These are generated through combinations of lateral translation of vertical stackings, as illustrated in Fig. 1.

The AA stacking is formed by directly placing one monolayer atop the other with perfect registry of atomic positions, preserving the out-of-plane mirror symmetry  $M_z$  in the *xy*-plane. The AB and BA configurations are obtained from AA by laterally translating the upper layer by fractional vectors  $\mathbf{t}_1 = (-1/3, -2/3)$  and  $\mathbf{t}_2 = (1/3, 2/3)$  in units of the primitive lattice vectors, respectively. Note that the BA stacking is equivalently obtained by a 180° rotation of the AB configuration about the *y*-axis.

The optimized interlayer distances  $d_{\perp}$  and stacking energies  $E_{\text{stack}}$  (defined as  $E_{\text{stack}} = E_{\text{bilayer}} - 2E_{\text{monolayer}}$  per formula unit) are summarized in Table I. The AA stack-

ing exhibits the largest interlayer separation ( $d_{\perp} \approx 3.75$  Å), consistent with weak van der Waals binding and minimal orbital overlap in eclipsed iodine positions. In contrast, translational shifts in AB and BA reduce  $d_{\perp}$  to  $\sim 3.45$  Å, indicating enhanced interlayer cohesion due to staggered iodine alignment.

Among the three configurations, AB configuration emerges as the lowest-energy structure, with  $E_{\text{stack}} = -0.22$  eV/f.u. and BA configuration has a comparable energy. The AA configuration has a little higher energy  $-0.18$  eV/f.u. These structural variations lay the foundation for the observed diversity in interlayer magnetic coupling, as discussed in subsequent sections.

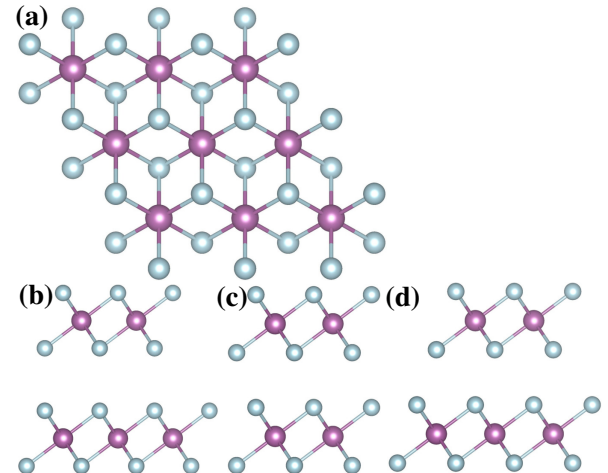


FIG. 1. (a) Top view of monolayer ScI<sub>2</sub>. Side view of bilayer ScI<sub>2</sub> showing three distinct stacking configurations: (b)BA, (c) AA, and (d)AB. Scandium and iodine atoms are represented in violet and grey, respectively.

### B. Electronic structure of monolayer and bilayer ScI<sub>2</sub>

Following the structural optimization of monolayer and bilayer ScI<sub>2</sub> in different stacking configurations, we now analyze their electronic structures to establish a reference for the stacking-dependent magnetic interactions discussed in subsequent sections. Electronic band structures and densities of states (DOS) were calculated for the optimized geometries, with emphasis on qualitative trends in orbital character and stacking-induced mod-

TABLE I. Optimized interlayer distance  $d_{\perp}$  and stacking energy  $E_{\text{stack}}$  (per formula unit) for different bilayer configurations of ScI<sub>2</sub>.

Configuration	$d_{\perp}$ (Å)	$E_{\text{stack}}$ (eV/f.u.)
AA	3.38	-0.18
AB	3.40	-0.22
BA	4.05	-0.21

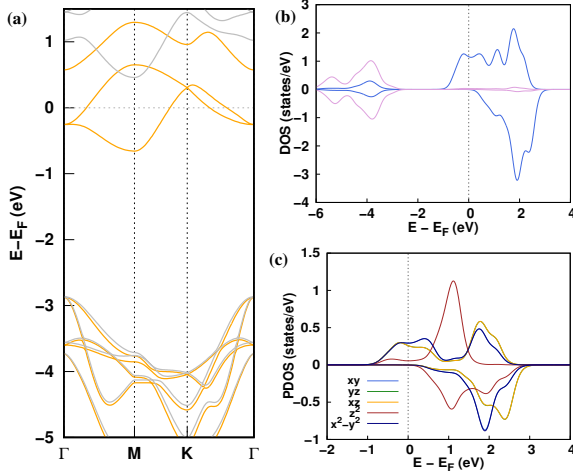


FIG. 2. Electronic structure of monolayer  $\text{ScI}_2$ . (a) Spin-polarized band structure along high-symmetry directions of the Brillouin zone. (b) Spin-polarized density of states showing contributions from  $\text{Sc-}d$  and  $\text{I-}p$  orbitals. (c) Spin-polarized density of states projected on the five  $d$  orbitals of  $\text{Sc}$ . The Fermi level ( $E_F$ ) is set to zero of the energy axis.

ifications in the electronic structure. The monolayer  $\text{ScI}_2$  exhibits a spin-polarized electronic structure dominated by  $\text{Sc-}d$  states near the Fermi level, as shown in Fig. 2. Owing to the nominal  $\text{Sc}^{2+}$  valence state with a single  $d$  electron, only one majority-spin band crosses the Fermi level, while the minority-spin channel remains gapped. This electronic configuration clearly indicates the half-metallic nature of monolayer  $\text{ScI}_2$ . The projected DOS further confirms that the electronic states in the immediate vicinity of the Fermi energy ( $E_F$ ) arise predominantly from  $\text{Sc-}d$  orbitals, whereas the  $\text{I-}p$  states are located at significantly lower energies, approximately 4 eV below ( $E_F$ ), and exhibit appreciable hybridization with the  $\text{Sc-}d$  states.

Such narrow  $d$ -derived bands close to the Fermi level are a common feature of two-dimensional transition-metal magnetic systems and reflect the reduced dimensionality and relatively localized nature of the transition-metal  $d$  electrons [1, 26, 27]. The calculated band structure of monolayer  $\text{ScI}_2$  shows moderately dispersive bands, consistent with this picture and with previous first-principles studies on related two-dimensional magnetic halides[28, 29].

When two  $\text{ScI}_2$  layers are combined to form bilayers, the overall electronic structure remains qualitatively similar to that of the monolayer; however, clear stacking-dependent modifications emerge. While the intralayer electronic features are largely preserved, the relative lateral displacement between the layers in AA, AB, and BA stackings alters the degree of interlayer orbital overlap. Fig. 3 (lower panel) shows that subtle changes in band dispersion near the Fermi level, particularly for bands with dominant  $\text{Sc-}d$  character. These variations indicate stacking-sensitive interlayer hybridization without lead-

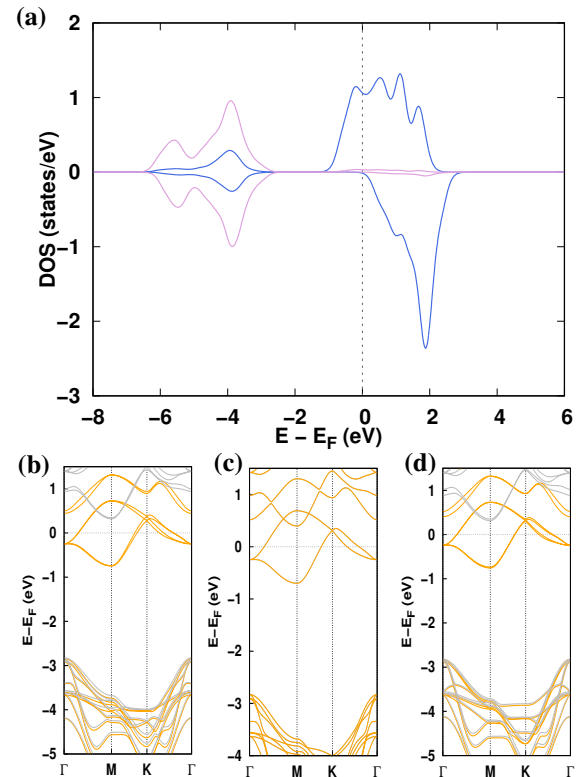


FIG. 3. Stacking-dependent electronic structure of bilayer  $\text{ScI}_2$ . (a) Projected density of states for the AA-stacked bilayer, highlighting  $\text{Sc-}d$  and  $\text{I-}p$  orbital contributions. (b) Spin-polarized band structures for AA, AB, and BA stacking configurations. Orange (grey) bands present the majority (minority) spin channel. The Fermi level is set to zero of the energy axis.

ing to a drastic reconstruction of the electronic structure, confirming that the bilayers retain their quasi-two-dimensional nature.

A closer inspection of the projected DOS in Fig. 3(a) shows that stacking-induced changes primarily affect the  $\text{Sc-}d$  states, which play a central role in determining the magnetic exchange interactions. The  $\text{I-}p$  states continue to act as mediators of hybridization, forming  $\text{Sc-I-Sc}$  pathways both within and across layers. Depending on the stacking configuration, the relative alignment of  $\text{Sc}$  and  $\text{I}$  atoms across the interface modifies these hybridization channels, leading to stacking-dependent electronic fingerprints near  $E_F$ . Although these differences are modest in the electronic spectra, they have important consequences for the sign and magnitude of interlayer magnetic exchange interactions, as discussed in the following section.

It should be emphasized that the present analysis does not aim at bandgap engineering or precise determination of electronic gaps. In low-dimensional and correlated systems, bandgap values are known to be sensitive to the choice of exchange-correlation functional, the Hubbard  $U$  parameter[28], and many-body correc-

tions beyond standard density functional theory [30–32]. Previous studies employing advanced approaches such as GW and related methods have demonstrated substantial quantitative corrections to DFT band gaps in two-dimensional materials [30, 31]. In this context, the present focus on robust qualitative trends in orbital character and stacking-dependent electronic modifications provides a physically transparent and reliable basis for understanding the magnetic behavior of bilayer  $\text{ScI}_2$ .

### C. Magnetic exchange interactions

The stacking-dependent magnetic behavior of bilayer  $\text{ScI}_2$  is governed by the nature and strength of magnetic exchange interactions within and between the layers. To quantify these interactions, total energies obtained from first-principles calculations were mapped onto an effective Heisenberg spin Hamiltonian of the form

$$H = - \sum_{\langle ij \rangle} J_{ij} \mathbf{S}_i \cdot \mathbf{S}_j, \quad (7)$$

where  $J_{ij}$  denotes the magnetic exchange coupling between spins  $\mathbf{S}_i$  and  $\mathbf{S}_j$ , and the summation runs over relevant intra- and interlayer neighbor pairs. Within this convention, positive (negative) values of  $J_{ij}$  correspond to ferromagnetic (antiferromagnetic) exchange interactions.

For monolayer  $\text{ScI}_2$ , the magnetic interaction is dominated by the nearest-neighbor (1NN) intralayer exchange between localized Sc moments. From the DFT calculations, the 1NN intralayer exchange constant is estimated to be  $J_{\parallel}^{\text{1NN}} = 33.2$  meV, indicating a strong ferromagnetic coupling within a monolayer. This relatively large energy scale is consistent with the narrow Sc-*d*-derived bands near the Fermi level and serves as the reference interaction strength for the bilayer systems. In the bilayer calculations, the intralayer exchange interaction is found to remain nearly unchanged, reflecting the weak influence of interlayer van der Waals bonding on the intrinsic magnetic coupling within each layer.

In contrast, the interlayer magnetic exchange interaction exhibits a pronounced dependence on the stacking configuration. By comparing total energies corresponding to ferromagnetic and antiferromagnetic alignments of the magnetic moments in the two layers, both nearest-neighbor (1NN) and second- nearest-neighbor (2NN) interlayer exchange interactions were extracted. The resulting exchange constants for all stacking configurations are summarized in Table II. For the AA-stacked bilayer, the 1NN interlayer exchange interaction is ferromagnetic with a value of 0.93 meV, while the corresponding 2NN interaction amounts to 0.17 meV. In the AB-stacked configuration, both 1NN and 2NN interlayer exchange interactions become antiferromagnetic, with values of  $-0.27$  meV and  $-0.13$  meV, respectively. For the BA stacking,

the interlayer exchange reverts to a ferromagnetic character, with 1NN and 2NN exchange constants of 0.16 meV and 0.083 meV, respectively.

As summarized in Table II, these results clearly demonstrate that the sign and magnitude of the interlayer magnetic exchange in bilayer  $\text{ScI}_2$  can be tuned by relative lateral displacement of the layers. The stacking-dependent reversal between ferromagnetic and antiferromagnetic interlayer coupling can be traced back to modifications in interlayer Sc–I–Sc exchange pathways, as discussed in the electronic structure section. Although the interlayer exchange interactions are an order of magnitude smaller than the intralayer coupling, they play a decisive role in determining the magnetic ground state and finite- temperature magnetic ordering of the bilayer system.

TABLE II. Interlayer magnetic exchange interactions, first nearest neighbor (1NN) and second nearest neighbor (2NN), for different configurations of  $\text{ScI}_2$ . Positive (negative) values indicate ferromagnetic (antiferromagnetic) coupling.

Config.	Magnetic exchange interaction in meV	
	1NN	2NN
AA	0.93	0.17
AB	-0.27	-0.13
BA	0.16	0.08

### D. Magnetic anisotropy energy

While the stacking-dependent interlayer exchange interactions discussed in the previous section determine the relative alignment of magnetic moments across the layers, magnetic anisotropy plays a complementary role by stabilizing long-range magnetic order in low-dimensional systems. The presence of a finite magnetic anisotropy energy (MAE) lifts the continuous spin-rotational symmetry and suppresses long-wavelength spin fluctuations, thereby enabling finite-temperature magnetic ordering. In this context, we examine the MAE of monolayer and bilayer  $\text{ScI}_2$  and its dependence on stacking configuration.

The MAE was evaluated by including spin–orbit coupling within the noncollinear density functional theory framework and computing the total energy difference between different magnetization orientations. Specifically, the MAE is defined as

$$\Delta E_{\text{MAE}} = E_{110} - E_{001}, \quad (8)$$

where  $E_{110}$  and  $E_{001}$  denote the total energies with magnetization oriented along the in-plane [110] and out-of-plane [001] directions, respectively. Within this convention, a positive MAE corresponds to an in-plane magnetic easy axis.

For monolayer  $\text{ScI}_2$ , the calculated MAE is 0.07 eV per formula unit, indicating a well- defined magnetic easy

axis along the out-of-plane [001] direction. This relatively large anisotropy reflects the combined effects of reduced dimensionality and spin-orbit coupling, primarily originating from the heavy iodine atoms. Together with the strong intralayer ferromagnetic exchange interaction discussed earlier, this out-of-plane anisotropy supports the stabilization of long-range magnetic order in the monolayer system.

Importantly, the bilayer  $\text{ScI}_2$  systems exhibit a qualitatively similar anisotropic behavior. For the AA, AB, and BA stacking configurations, the calculated MAE values are 0.05, 0.06, and 0.05 eV per formula unit, respectively. In all three cases, the MAE remains positive, indicating that the magnetic easy axis continues to lie along the out-of-plane [001] direction. The relatively small variation of MAE among different stacking configurations suggests that magnetic anisotropy in bilayer  $\text{ScI}_2$  is only weakly affected by stacking geometry, in contrast to the pronounced stacking dependence observed for the interlayer exchange interactions.

The persistence of out-of-plane magnetic anisotropy from monolayer to bilayer  $\text{ScI}_2$  indicates that interlayer coupling does not significantly alter the spin-orbit-induced anisotropic energy landscape. Although the magnitude of the MAE is slightly reduced in the bilayer compared to the monolayer, it remains sufficiently large to stabilize long-range magnetic order. The MAE values obtained here, together with the exchange parameters discussed in the previous section, provide the essential input parameters for the Monte Carlo simulations used to estimate the magnetic ordering temperatures, which are presented in the following section.

### E. Finite-temperature magnetic ordering and Monte Carlo simulations

The magnetic exchange parameters and magnetic anisotropy energies obtained from first-principles calculations provide the microscopic basis for assessing the finite-temperature magnetic behavior of bilayer  $\text{ScI}_2$ . While density functional theory is inherently restricted to zero temperature, the stability of magnetic order against thermal fluctuations can be reliably examined using finite-temperature Monte Carlo simulations. In the present work, classical Monte Carlo simulations were carried out for bilayer  $\text{ScI}_2$  in the AA, AB, and BA stacking configurations, using exchange parameters derived from first-principles calculations and incorporating the out-of-plane magnetic anisotropy discussed in the previous section.

The temperature dependence of the magnetization and magnetic susceptibility was evaluated for several system sizes to characterize the nature of the magnetic phase transitions. For the AA- and BA-stacked bilayers, which exhibit ferromagnetic ground states, the magnetization decreases rapidly with increasing temperature and vanishes near a well-defined critical temperature, signaling

a transition from an ordered ferromagnetic phase to a paramagnetic state. In the same temperature range, the magnetic susceptibility displays a pronounced peak, providing an initial estimate of the ordering temperature. These features are clearly visible in the temperature-dependent magnetization and susceptibility curves shown in Fig. 4(a-f).

In contrast, the AB-stacked bilayer stabilizes an antiferromagnetic ground state, resulting in a strongly suppressed net magnetization over the entire temperature range due to the antiparallel alignment of spins in the two layers. Consequently, the thermal response of the AB stacking is not characterized by a finite total magnetization but is instead reflected through enhanced magnetic fluctuations and corresponding features in the susceptibility. This qualitative distinction between ferromagnetic and antiferromagnetic stackings is consistently captured by the Monte Carlo simulations and mirrors the magnetic ground states predicted from first-principles calculations.

A more accurate and size-independent determination of the magnetic ordering temperature is obtained from the analysis of the fourth-order Binder cumulant calculated for multiple system sizes. The crossing points of the Binder cumulant curves within a narrow temperature window provide a robust estimate of the critical temperature, as shown in Fig. 4(g-i). This analysis confirms the presence of long-range ferromagnetic order in the AA and BA stackings and the absence of a net magnetization in the antiferromagnetic AB configuration, while still allowing a well-defined thermal transition to be identified.

The critical temperatures extracted from the Binder cumulant crossings are found to lie in the range of approximately 360–375 K for all three stacking configurations and are summarized in Table III. Notably, despite the distinct magnetic ground states and stacking-dependent interlayer exchange interactions, the ordering temperatures remain remarkably similar across all configurations. This observation indicates that the dominant energy scale governing the thermal stability of magnetic order is the strong intralayer exchange interaction, whereas the stacking-dependent interlayer coupling primarily determines the nature of the magnetic ground state rather than the magnitude of the transition temperature.

To estimate the transition temperature in the thermodynamic limit, a finite-size scaling analysis was performed using the Binder-cumulant-derived critical temperatures for different system sizes. The thermodynamic-limit transition temperature  $T_c(\infty)$  was obtained by fitting the finite-size estimates  $T_c(L)$  using the scaling relation

$$T_c(L) = T_c(\infty) + aL^{-1/\nu}, \quad (9)$$

where  $L$  is the linear system size and  $\nu$  is the correlation-length exponent[33]. Given the quasi-two-dimensional Ising-like nature of the system enforced by the strong out-of-plane magnetic anisotropy, the exponent was taken as  $\nu = 1$ , leading to a linear dependence on  $1/L$ . A weighted linear fit, with weights determined by the statistical un-

TABLE III. Critical temperatures  $T_c$  obtained from Binder cumulant crossings for different stacking configurations of bilayered  $\text{ScI}_2$ . The corresponding magnetic ground states are also indicated.

Stacking	Magnetic order	$T_c$ (K)
AA	Ferromagnetic	$370.0 \pm 5.8$
AB	Antiferromagnetic	$371.9 \pm 6.8$
BA	Ferromagnetic	$369.4 \pm 3.5$

certainties of the Binder cumulant crossings, yields a reliable estimate of the transition temperature in the thermodynamic limit. Such a statistical estimation of  $T_c$  is indeed reliable in 2D magnetic systems [34].

Overall, the Monte Carlo simulations demonstrate that bilayer  $\text{ScI}_2$  sustains robust magnetic order at and above room temperature for all considered stacking configurations. At the same time, the magnetic ground state—ferromagnetic or antiferromagnetic—can be selectively tuned through stacking geometry without significantly affecting the ordering temperature. This combination of high thermal stability and stacking-controlled magnetic order underscores the potential of bilayer  $\text{ScI}_2$  as a model platform for exploring tunable magnetism in two-dimensional van der Waals materials.

The stacking-dependent interlayer magnetic coupling observed in bilayer  $\text{ScI}_2$  reflects a general mechanism operative in layered magnetic materials, in which subtle changes in atomic registry qualitatively modify superexchange pathways. In such systems, local magnetic moments typically originate from partially filled transition-metal  $d$  orbitals, while ligand  $p$  orbitals mediate magnetic interactions through virtual hopping processes. Consequently, the sign and magnitude of the interlayer exchange interaction are governed not only by the interlayer distance but, more critically, by the symmetry and orbital overlap along the metal–ligand–metal exchange paths, which are directly controlled by stacking geometry.

In the AA and BA stacking configurations, the relative alignment of the layers favors interlayer superexchange pathways characterized by near-orthogonal overlap between the dominant  $\text{Sc-}d$  orbitals and  $\text{I-}p$  orbitals across the interface. Within the Goodenough–Kanamori–Anderson framework, such geometries suppress antiferromagnetic kinetic exchange and allow ferromagnetic superexchange contributions, often stabilized by Hund’s coupling on the ligand  $p$  orbitals [35–37]. As a result, the effective interlayer exchange interaction remains ferromagnetic in these stackings. Importantly, this mechanism does not rely on direct interlayer metal–metal overlap but arises from the symmetry of the metal–ligand–metal exchange paths, making it broadly applica-

ble to van der Waals magnets with similar bonding motifs.

In contrast, the AB stacking introduces a registry in which the relative lateral displacement of the layers enhances symmetry-allowed overlap between compatible  $\text{Sc-}d$  and  $\text{I-}p$  orbitals across the interface. This configuration promotes virtual hopping processes that favor antiparallel spin alignment, thereby stabilizing antiferromagnetic superexchange in accordance with the Goodenough–Kanamori–Anderson rules [35, 37]. Similar stacking- and registry-driven reversals of interlayer magnetic coupling have been reported in other two-dimensional magnetic systems, including transition-metal halides and related van der Waals magnets [1, 26, 27].

From a broader perspective, the coexistence of stacking-sensitive interlayer exchange and stacking-insensitive intralayer magnetism highlights a general design principle for two-dimensional magnetic materials. While strong intralayer exchange interactions set the dominant energy scale and govern the magnetic ordering temperature, stacking geometry provides an efficient and reversible handle for tuning the magnetic ground state. This separation of energy scales explains why stacking can switch between ferromagnetic and antiferromagnetic interlayer order without significantly affecting the thermal stability of magnetism, as observed here and anticipated in a wider class of layered van der Waals magnets.

#### IV. CONCLUSIONS

In summary, we have carried out a comprehensive first-principles and finite-temperature study of stacking-dependent magnetic ordering in bilayer  $\text{ScI}_2$ . Using density functional theory combined with Hubbard- $U$  corrections, we systematically analyzed the structural, electronic, and magnetic properties of monolayer and bilayer  $\text{ScI}_2$  in three distinct stacking configurations. The electronic structure calculations reveal a spin-polarized ground state dominated by  $\text{Sc-}d$  states near the Fermi level, providing the microscopic origin of magnetism in this system.

By mapping total energies onto an effective Heisenberg spin Hamiltonian, we demonstrated that while the strong intralayer ferromagnetic exchange interaction remains largely unaffected by stacking, the interlayer magnetic exchange is highly sensitive to the relative stacking geometry. Specifically, AA and BA stackings favor ferromagnetic interlayer coupling, whereas the AB stacking stabilizes an antiferromagnetic interlayer alignment. Magnetic anisotropy calculations further show that both monolayer and bilayer  $\text{ScI}_2$  possess a robust out-of-plane magnetic easy axis, ensuring the stability of long-range magnetic order in this quasi-two-dimensional system.

Finite-temperature Monte Carlo simulations based on the DFT-derived exchange parameters and anisotropy energies reveal that bilayer  $\text{ScI}_2$  sustains magnetic or-

dering at and above room temperature for all considered stacking configurations. Despite the stacking-dependent magnetic ground states, the ordering temperatures are found to lie within a narrow range, highlighting the dominant role of intralayer exchange in controlling thermal stability. Binder cumulant analysis and finite-size scaling further confirm the robustness of these transition temperatures in the thermodynamic limit.

The combination of high magnetic ordering temperature, stacking-tunable interlayer magnetism, and robust magnetic anisotropy makes bilayer  $\text{ScI}_2$  a promising platform for exploring controllable magnetism in two-dimensional van der Waals materials. From an application perspective, the ability to switch between ferromagnetic and antiferromagnetic interlayer coupling through stacking geometry may be exploited in spintronic and magneto-electronic devices, such as spin-filtering junctions and stacking-engineered magnetic heterostructures. Future studies may extend the present work by exploring the effects of external stimuli such as strain, electric

fields, or carrier doping, as well as by incorporating more advanced many-body treatments to refine the description of electronic correlations. Experimental validation of stacking-dependent magnetic behavior in bilayer  $\text{ScI}_2$  would further advance the understanding of tunable magnetism in layered materials.

## ACKNOWLEDGMENTS

This work was supported by the Anusandhan National Research Foundation (formerly Science and Engineering Research Board) for the computational support through the start-up research grant (SRG/2023/000122).

## DATA AVAILABILITY STATEMENT

Data sets generated during the current study are available from the corresponding author on reasonable request.

- 
- [1] K. S. Burch, D. Mandrus, and J.-G. Park, Magnetism in two-dimensional van der Waals materials, *Nature* **563**, 47 (2018).
  - [2] Y. Li, X. Gao, Z. Huang, Y. Liu, Y. Liu, J. Wang, S. Li, and X. Duan, Recent advances in 2D van der Waals magnets, *iScience* **26**, 107649 (2023).
  - [3] N. Sivadas, S. Okamoto, D. Xiao, and X. Xu, Stacking-Dependent Magnetism in Bilayer  $\text{CrI}_3$ , *Nano Letters* **18**, 7658 (2018).
  - [4] P. Jiang, C. Wang, D. Chen, Z. Zhong, Z. Yuan, Z.-Y. Lu, and W. Ji, Stacking tunable interlayer magnetism in bilayer  $\text{CrI}_3$ , *Physical Review B* **99**, 144401 (2019).
  - [5] S.-H. Park, S.-H. Chae, J. H. Moon, S.-H. Baek, S. Jung, K.-J. Kim, J.-W. Kim, D.-Y. Kim, D.-H. Kim, J.-S. Choi, B.-C. Min, and J. W. Choi, Layer-dependent magnetic phases of  $\text{Fe}_3\text{GeTe}_2$ , *Physical Review B* **105**, 014406 (2022).
  - [6] N.-W. Wang, Y.-J. Zhang, X.-H. Lv, X.-L. Zhao, P.-L. Gong, C.-D. Jin, J.-L. Wang, and X.-Q. Shi, Interlayer magnetic transition in van der Waals  $d^1$  correlated magnets: A perspective from interlayer band coupling, *Physical Review B* **110**, 245420 (2024).
  - [7] S. Jiang, L. Li, Z. Wang, J. Shan, and K. F. Mak, Recent progress on 2D magnets: Fundamental mechanism, structural design and modification, *Applied Physics Reviews* **8**, 031305 (2021).
  - [8] T. Song, X. Cai, M. W.-Y. Tu, X. Zhang, B. Huang, S. P. Wilson, K. L. Seyler, L. Zhu, T. Taniguchi, K. Watanabe, M. A. McGuire, D. Xiao, W. Yao, and X. Xu, Direct observation of van der Waals stacking-dependent interlayer magnetism, *Science* **365**, 1434 (2019).
  - [9] S. Yang, X. Xu, B. Han, P. Gu, R. Guzman, Y. Song, Z. Lin, P. Gao, W. Zhou, J. Yang, Z. Chen, and Y. Ye, Controlling the 2D Magnetism of  $\text{CrBr}_3$  by van der Waals Stacking Engineering, *Journal of the American Chemical Society* **145**, 28184 (2023).
  - [10] W. Sun, H. Ye, L. Liang, N. Ding, S. Dong, and S.-S. Wang, Stacking-dependent ferroicity of a reversed bilayer: Altermagnetism or ferroelectricity, *Physical Review B* **110**, 224418 (2024).
  - [11] Y. Ga, F. Zhang, L. Wang, J. Jiang, K. Chang, and H. Yang, Interlayer exchange coupling driven magnetic phase transition in a two-dimensional lattice, *Physical Review B* **112**, L020407 (2025).
  - [12] J. B. Goodenough, Theory of the Role of Covalence in the Perovskite-Type Manganites  $[\text{La}, \text{M(II)}]\text{MnO}_3$ , *Physical Review* **100**, 564 (1955).
  - [13] J. Kanamori, Superexchange interaction and symmetry properties of electron orbitals, *Journal of Physics and Chemistry of Solids* **10**, 87 (1959).
  - [14] Y. Nomura and R. Arita, A structure map for  $\text{AB}_2$  type 2D materials using high-throughput DFT calculations, *Materials Advances* **2**, 5715 (2021).
  - [15] C. M. Acosta, E. Ogoshi, J. A. Souza, G. M. Dalpian, A. Zunger, and A. Fazzio, Machine Learning Study of the Magnetic Ordering in 2D Materials, *ACS Applied Materials & Interfaces* **14**, 10285 (2022).
  - [16] P. Giannozzi, S. Baroni, N. Bonini, M. Calandra, R. Car, C. Cavazzoni, D. Ceresoli, G. L. Chiarotti, M. Cococcioni, I. Dabo, *et al.*, Quantum espresso: a modular and open-source software project for quantum simulations of materials, *Journal of Physics: Condensed Matter* **21**, 395502 (2009).
  - [17] P. Giannozzi, O. Andreussi, T. Brumme, O. Bunau, M. Buongiorno Nardelli, M. Calandra, R. Car, C. Cavazzoni, D. Ceresoli, M. Cococcioni, *et al.*, Advanced capabilities for materials modelling with quantum espresso, *Journal of Physics: Condensed Matter* **29**, 465901 (2017).
  - [18] J. P. Perdew, K. Burke, and M. Ernzerhof, Generalized gradient approximation made simple, *Physical Review Letters* **77**, 3865 (1996).

- [19] P. E. Blöchl, Projector augmented-wave method, *Physical Review B* **50**, 17953 (1994).
- [20] H. J. Monkhorst and J. D. Pack, Special points for brillouin-zone integrations, *Physical Review B* **13**, 5188 (1976).
- [21] S. L. Dudarev, G. A. Botton, S. Y. Savrasov, C. J. Humphreys, and A. P. Sutton, Electron-energy-loss spectra and the structural stability of nickel oxide: An LSDA+U study, *Physical Review B* **57**, 1505 (1998).
- [22] Y. Wu, J. Tong, L. Deng, F. Luo, F. Tian, G. Qin, and X. Zhang, Realizing spontaneous valley polarization and topological phase transitions in monolayer  $ScX_2$  (X=Cl, Br, I), *Acta Materialia* **246**, 118731 (2023).
- [23] S. Grimme, J. Antony, S. Ehrlich, and H. Krieg, A consistent and accurate ab initio parametrization of density functional dispersion correction (DFT-D) for the 94 elements (H-Pu), *J. Chem. Phys.* **132**, 154104 (2010).
- [24] M. Matsuura and Y. Ajiro, Crystallographic Two Sublattice System –Staggered Susceptibility and Induced Staggered Magnetization in Paramagnetic State, *Journal of the Physical Society of Japan* **41**, 44 (1976).
- [25] Y. Xu, Y. Li, X. Chen, C. Zhang, R. Zhang, and P. Lu, First-principle study of hydrogenation on monolayer  $MoS_2$ , *AIP Advances* **6**, 075001 (2016).
- [26] C. Gong, L. Li, Z. Li, and et al., Discovery of intrinsic ferromagnetism in two-dimensional van der waals crystals, *Nature* **546**, 265 (2017).
- [27] B. Huang, G. Clark, E. Navarro-Moratalla, D. R. Klein, R. Cheng, K. L. Seyler, D. Zhong, E. Schmidgall, M. A. McGuire, D. H. Cobden, W. Yao, D. Xiao, P. Jarillo-Herrero, and X. Xu, Layer-dependent ferromagnetism in a van der Waals crystal down to the monolayer limit, *Nature* **546**, 270 (2017).
- [28] S. Sarkar and P. Kratzer, Electronic correlation, magnetic structure, and magnetotransport in few-layer  $CrI_3$ , *Physical Review Materials* **4**, 104006 (2020).
- [29] S. Sarkar and P. Kratzer, Magnetic exchange interactions in bilayer  $CrX_3$  (X=Cl, Br and I): A critical assessment of the DFT+ $U$  approach, *Physical Review B* **103**, 224421 (2021).
- [30] D. Y. Qiu, F. H. da Jornada, and S. G. Louie, Optical Spectrum of  $MoS_2$  Many-Body Effects and Diversity of Exciton States, *Physical Review Letters* **111**, 216805 (2013).
- [31] A. Ramasubramaniam, Large excitonic effects in monolayers of molybdenum and tungsten dichalcogenides, *Physical Review B* **86**, 115409 (2012).
- [32] M. S. Hybertsen and S. G. Louie, Electron correlation in semiconductors and insulators: Band gaps and quasiparticle energies, *Physical Review B* **34**, 5390 (1986).
- [33] I. Diaz and N. Branco, Monte Carlo simulations of an Ising bilayer with non-equivalent planes, *Physica A: Statistical Mechanics and its Applications* **468**, 158 (2017).
- [34] S. Chandra, Compensation and its systematics in spin-1/2 Ising trilayered triangular ferrimagnet, *Journal of Physics and Chemistry of Solids* **156**, 110165 (2021).
- [35] J. B. Goodenough, *Magnetism and the Chemical Bond*, Inorganic Chemistry Section / Interscience monographs on chemistry (Interscience, 1963).
- [36] J. Kanamori, Superexchange interaction and symmetry properties of electron orbitals, *Journal of Physics and Chemistry of Solids* **10**, 87 (1959).
- [37] P. W. Anderson, New approach to the theory of superexchange interactions, *Phys. Rev.* **115**, 2 (1959).

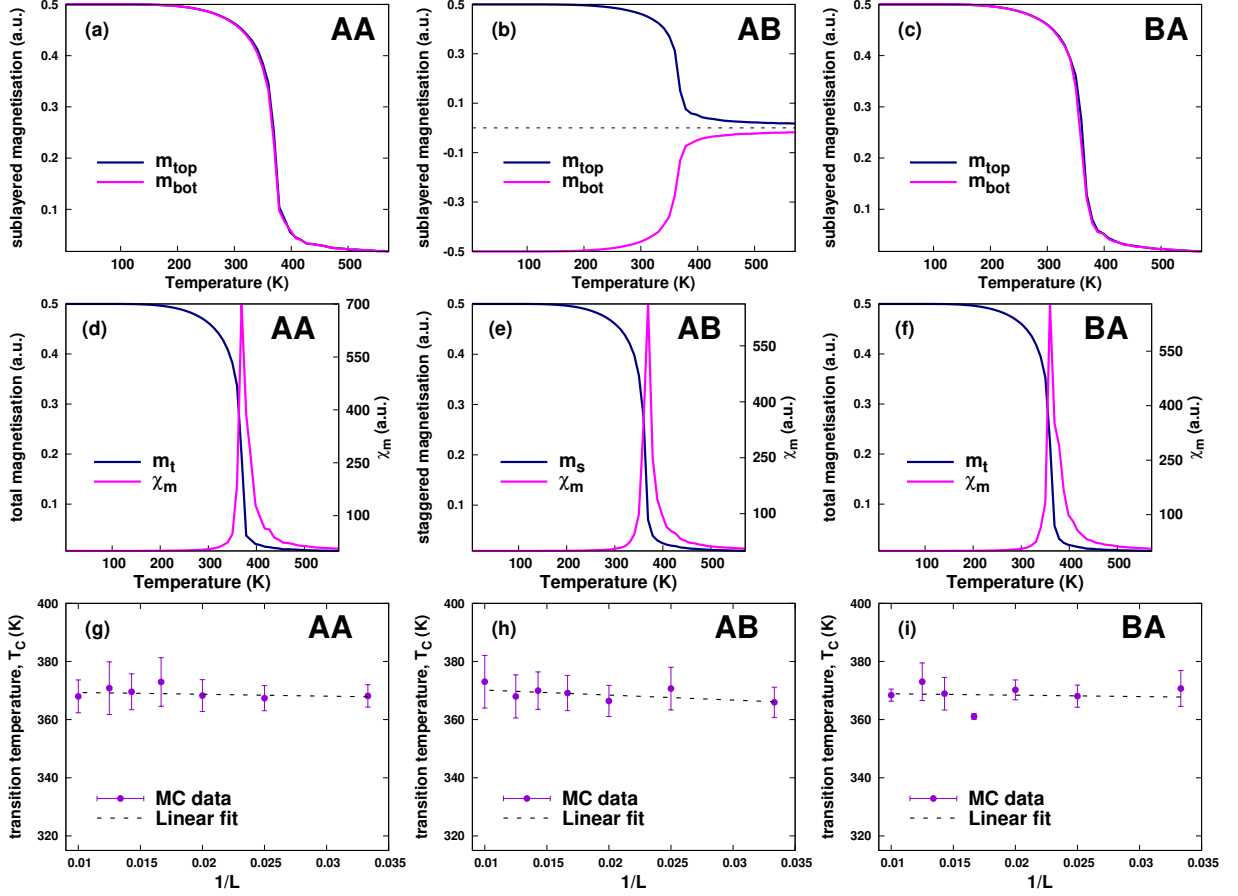


FIG. 4. Finite-size scaling analysis of the magnetic transition temperature in bilayer  $\text{ScI}_2$ . Panels (a)–(c) show the temperature dependence of the Binder cumulant  $U_L$  for different system sizes for the AA, AB, and BA stacking configurations, respectively. Panels (d)–(f) display the corresponding Binder cumulant crossings used to extract finite-size estimates of the transition temperature. The Monte Carlo simulations shown in panels (a)–(f) were performed on lattices with a linear dimension of  $L = 100$ . Panels (g)–(h) present the weighted linear extrapolation of the critical temperature  $T_c$  as a function of  $1/L$ , where the intercept yields the transition temperature in the thermodynamic limit.